Observations of SST-Induced Perturbations of the Wind Stress Field over the Southern Ocean on Seasonal Timescales

LARRY W. O'NEILL, DUDLEY B. CHELTON, AND STEVEN K. ESBENSEN

College of Oceanic and Atmospheric Sciences, Oregon State University, Corvallis, Oregon

(Manuscript received 5 August 2002, in final form 13 January 2003)

ABSTRACT

The surface wind stress response to sea surface temperature (SST) over the latitude range 30°–60°S in the Southern Ocean is described from the National Aeronautics and Space Administration's QuikSCAT scatterometer observations of wind stress and Reynolds analyses of SST during the 2-yr period August 1999 to July 2001. While ocean–atmosphere coupling at midlatitudes has previously been documented from several case studies, this is the first study to quantify this relation over the entire Southern Ocean. The spatial structures of the surface wind perturbations with wavelengths shorter than 10° latitude by 30° longitude are closely related to persistent spatial variations of the SST field on the same scales. The wind stress curl and divergence are shown to be linearly related, respectively, to the crosswind and downwind components of the SST gradient. The curl response has a magnitude only about half that of the divergence response. This observed coupling is consistent with the hypothesis that SST modification of marine atmospheric boundary layer (MABL) stability affects vertical turbulent mixing of momentum, inducing perturbations in the surface winds. The nonequivalence between the responses of the curl and divergence to the crosswind and downwind SST gradients suggests that secondary circulations in the MABL may also play an important role by producing significant perturbations in the surface wind field near SST fronts that are distinct from the vertical turbulent transfer of momentum. The importance of the wind stress curl in driving Ekman vertical velocity in the open ocean implies that the coupling between winds and SST may have important feedback effects on upper ocean processes near SST fronts.

1. Introduction

The response of the near-surface wind field to underlying sea surface temperature (SST) gradients has been investigated in the eastern tropical Pacific in several recent studies from analyses of satellite observations of winds and SST (Chelton et al. 2001; Liu et al. 2000; Hashizume et al. 2001; Polito et al. 2001). The broad spatial coverage and high temporal resolution of the satellite datasets have allowed a quantitative test of the coupling between SST and surface winds hypothesized by Wallace et al. (1989) from climatological SST and wind data. Chelton et al. (2001) showed that this coupling is most clearly manifested in the wind stress curl and divergence fields, which were found to be linearly related to the crosswind and downwind components of the underlying SST gradient field, respectively. SST-induced perturbations of the wind stress, wind stress curl, and wind stress divergence were also shown to travel along with the surface SST signatures of the westward-propagating tropical instability waves (TIWs), providing statistically quantitative evidence of the rapid response of the near-surface wind field to the underlying spatially and temporally varying SST field. The eastern tropical Pacific analysis of Chelton et al. (2001) is extended in this study to investigate ocean–atmosphere coupling in regions of persistently strong SST gradients in the Southern Ocean.

Some issues pose challenges in extending the analysis of Chelton et al. (2001) to the Southern Ocean. First, the lack of high-quality SST data over the Southern Ocean is a fundamental limitation due to sparse in situ sampling and biases in satellite infrared measurements of SST. Second, the very energetic synoptic variability in the winds over the Southern Ocean tends to obscure the presence of the coupling between SST and surface winds. To address these concerns, the analysis presented here is based upon three-month averages of the analyzed SST fields produced by the National Oceanic and Atmospheric Administration (NOAA; Reynolds and Smith 1994) and the National Aeronautics and Space Administration (NASA) QuikSCAT scatterometer observations of surface wind stress.

Past observational and modeling studies of the effects of SST on near-surface winds are summarized in section 2. The data analyzed here and the motivation for using 3-month average wind stress and SST fields are described in section 3. The details of the analysis methods

Corresponding author address: Dr. Dudley B. Chelton, College of Oceanic and Atmospheric Sciences, Oregon State University, 104 Ocean Admin. Bldg., Corvallis, OR 97331-5503.
E-mail: chelton@coas.oregonstate.edu

are discussed in section 4. The results are presented in section 5 and discussion and conclusions are presented in section 6.

2. Background

Observations in midlatitudes clearly show that air flowing across SST fronts experiences changes in the air–sea heat flux and vertical turbulent mixing. In an early observational study, Sweet et al. (1981) found that surface winds intensified over the warmer water of the Gulf Stream, producing a visibly rougher ocean surface compared to the colder water closer to the coast. Throughout a series of aircraft flights, they reported turbulent flying conditions over the warmer water on the seaward side of the Gulf Stream and smooth conditions over the colder slope water. Smooth ocean waves on the cold water surface and whitecaps on the warm water surface exemplified the change in surface wind conditions associated with the SST front. From vertical profiles of atmospheric virtual potential temperature θ^* in the lower 600 m of the atmosphere, they showed that $\partial\theta^*/\partial z$ was positive over the colder water and negative over the warmer water, indicating stable and unstable conditions, respectively. Since stability influences vertical turbulent mixing through buoyancy, Sweet et al. (1981) suggested that the observed changes in wind speed across the front were caused by increased downward turbulent mixing of momentum from aloft to the surface over the warmer water. It is noteworthy that Sweet et al. (1981) found evidence of rising air over the warmer water and subsiding air over the cooler water in temperature and moisture patterns, suggestive of secondary circulations associated with the SST front.

Jury and Walker (1988) observed the same coupling between SST and surface winds from aerial surveys of the marine atmospheric boundary layer (MABL) across the the Agulhas Current south of Africa. Surface winds increased by 7 m s^{-1} in association with a 6°C change in SST over a distance of 400 km. They also found that turbulent momentum transfers over the warmer water were more efficient than over the colder water, reducing the magnitude of the vertical wind shear between the 70- and 300-m levels.

In a subsequent study from aircraft observations of winds across the northern edge of the Agulhas Current, Jury (1994) also found more efficient vertical turbulent mixing over warmer water than over the cooler, nearshore water. An SST increase of 8°C over a distance of 40 km was accompanied by a factor of 5 increase in surface wind stress. In addition, a 4-day composite average of the aircraft observations during Southern Hemisphere winter showed clear evidence of strong secondary circulations associated with the SST front.

Rouault and Lutjeharms (2000) further investigated the role of the SST on the overlying atmosphere south of Africa by measuring SST and atmospheric profiles of temperature, moisture, and wind from a ship survey across an SST front associated with the Agulhas Return Current. Over the colder water, they found lower wind speeds, increased atmospheric stability, and reduced air–sea heat fluxes compared to the warmer water. From coincident *European Remote Sensing Satellite-1* (*ERS-1*) scatterometer wind data, they also showed that the surface wind speed over a persistent warm-core eddy shed from the Agulhas Current was much higher than the wind speed over the surrounding colder water. Ship-based observations indicated that this occurred where the air–sea temperature difference created an unstable MABL, allowing increased vertical turbulent transport of momentum.

Midlatitude coupling between winds and SST has also been recently observed over the Kuroshio Extension by Nonaka and Xie (2003). Weekly averages of wind speed anomalies were found to be positively correlated with SST anomalies using wind speed measurements from a combination of QuikSCAT scatterometer data, satellite microwave imagers, and moored buoys. They also showed clear evidence that the wind speed anomalies propagated westward in phase with SST anomalies associated with westward-propagating meanders in the Kuroshio.

While observations have consistently found that the near-surface winds depend strongly on SST-induced stabilization of the MABL, Hsu (1984) proposed that another mechanism also contributes to wind variations over SST fronts. He showed analytically that temperature contrasts associated with SST fronts can induce secondary circulations perpendicular to the front, causing an acceleration of the surface winds across the front. Wai and Stage (1989) drew similar conclusions from a two-dimensional numerical model study of the northern edge of the Gulf Stream. In their model, secondary circulations developed over the SST front with rising air and low surface pressure over the warmer water and descending air and high surface pressure over the colder water. The associated cross-frontal surface pressure gradient was balanced by the vertical turbulent stress divergence. This balance caused the smallest surface wind stress to occur over the cold water; the wind stress increased across the front and then decreased gradually over the warm water.

Warner et al. (1990) obtained very similar results from a three-dimensional mesoscale model study of the Gulf Stream using realistic SST patterns. They found that the increased surface winds associated with cross-frontal secondary circulations enhance the surface heat fluxes, which further reinforces the secondary circulations. The Gulf Stream observations of Sweet et al. (1981) and the Agulhas observations of Jury (1994) are consistent with the secondary circulations and the associated pressure distribution found in the Wai and Stage (1989) and Warner et al. (1990) models.

Satellite observations in the tropical Pacific have documented the relationship between SST and surface winds in much greater detail than has been possible from

ship-based observations. As SST modification of surface winds has been studied more extensively in the tropical Pacific than at midlatitudes, we highlight here some important conclusions from the tropical Pacific that we believe have relevance to air–sea interaction in midlatitudes.

The near-surface wind response to SST gradients is especially clear in the Tropics because of the relatively weak signals of synoptic variability near the equator. Wallace et al. (1989) noted a weakening of the surface winds directly over the equatorial cold tongue in climatological average surface winds and SST. Cross-equatorial southerly winds increased over the warmer water north of the cold tongue with intensity dependent on the strength of the temperature contrast between the cold tongue and the warmer water to the north. Apparently unaware of the Gulf Stream observations by Sweet et al. (1981), Wallace et al. (1989) hypothesized independently that the principal mechanism for changing the surface winds is the modification of the vertical wind shear in the MABL through turbulent vertical momentum transport.

To investigate the relationship between the TIW-induced perturbations of SST and the surface winds hypothesized by Wallace et al. (1989), Hayes et al. (1989) analyzed time series of winds and SST measured from the Tropical Atmosphere Ocean (TAO) mooring array along 110°W at 2°N, 0°, and 2°S. Although the TAO mooring locations do not adequately resolve the zonal component of the surface wind divergence, Hayes et al. (1989) showed that latitudinal variations of the meridional component of the surface wind divergence correlated well with TIW-induced perturbations of the SST gradient field.

In the first satellite-based study of surface wind response to SST variability, Xie et al. (1998) showed that ERS-1 satellite scatterometer estimates of the 10-m surface wind field clearly resolved the coupling between TIW-induced perturbations of SST and surface winds. With the four-fold improvement in sampling (Schlax et al. 2001) and the presence of the well-developed cold tongue associated with the long-lasting La Niña conditions that developed after May 1998, QuikSCAT scatterometer observations of wind stress and Tropical Rainfall Measuring Mission (TRMM) Microwave Imager (TMI) observations of SST more vividly depicted these SST-induced perturbations of the surface wind field during the first 5 months of the QuikSCAT mission (Chelton et al. 2001; Liu et al. 2000; Hashizume et al. 2001). SST modification of the MABL is also evident in satellite measurements of clouds, columnar-integrated water vapor, and precipitation (Deser et al. 1993; Xie et al. 1998; Hashizume et al. 2001; Hashizume et al. 2002). Satellite and in situ buoy measurements show the effect of SST perturbations on the surface heat fluxes (Thum et al. 2002).

From ship-based observations along 2°N during September 1999, Hashizume et al. (2002) concluded that sea level pressure anomalies were too small to force the observed TIW-induced wind anomalies in the eastern tropical Pacific. Consistent with the hypothesis of Wallace et al. (1989), Hashizume et al. (2002) found that SST perturbations associated with the TIWs modulate the vertical wind shear through changes in MABL stability. During the TIW cold phase, they observed that strong temperature stratification suppressed vertical mixing. During the warm phase, the reduced MABL static stability allowed generation of vertical turbulent mixing that weakened the vertical wind shear. In response to increased SST during the warm phase, Hashizume et al. (2002) also found that the MABL warmed uniformly throughout, deepened significantly, and became capped by clouds. Due to the change in inversion height across the SST front, a dipole pattern of temperature anomalies developed vertically, with a warm anomaly below 1 km and a cold anomaly at the base of the inversion down to 1 km (the inversion height was above 1 km for the duration of the cruise). A positive hydrostatic pressure anomaly thus occurred near the top of the MABL that was compensated for by the negative hydrostatic pressure contribution from the warm layer below. Hashizume et al. (2002) found that the cancellation was almost complete from their soundings, reducing the sea level pressure anomalies expected for a MABL of constant depth.

The effects of sea level pressure anomalies in the equatorial Pacific were first investigated by Lindzen and Nigam (1987) using a simple one-layer model of the MABL. They proposed that variations in the MABL height across the cold tongue would reduce the sea level pressure gradient relative to what would occur within an MABL of constant depth. They further speculated that horizontal convergence and divergence of mass within the boundary layer modulate the hydrostatic pressure by changing the thickness of the MABL, with the ultimate effect of reducing the sea level pressure anomalies relative to those expected from an MABL with a rigid, flat top. The convergent mass would eventually exit the MABL into the bases of overlying cumulus clouds once the MABL reached a steady state. Since this mechanism reduces the cross-isotherm sea level pressure gradient from what would occur if the top of the MABL were rigid, Lindzen and Nigam (1987) describe this as a ''back pressure'' effect.

Hashizume et al. (2002) provided an alternative interpretation of the back pressure effect consistent with their observations of the MABL over the eastern tropical Pacific. They reconciled their TIW observations with the Lindzen and Nigam (1987) model by suggesting that the hydrostatic effects of temperature anomalies near the MABL top due to the deepening and shallowing mixed layer compensate for the effects of the warm and cool anomalies in the lower parts of the layer. Hashizume et al. (2002) propose that this compensation, rather than the horizontal mass adjustment hypothesized by Lindzen and Nigam (1987), causes the sea level pressure

over the warmer water to be smaller than expected from thermal heating considerations alone. This effect decreases the pressure gradient between the SST anomalies associated with the TIWs, suggesting that the turbulent transfer of momentum may be the dominant mechanism in SST-induced surface wind variations.

These various studies show that SST fronts significantly alter the entire MABL, not just the surface wind field. The hypothesized mechansims for changes in the surface wind field in the vicinity of SST fronts include vertical turbulent transport of momentum from aloft to the surface and pressure-induced secondary circulations. It is not possible to distinguish between these two mechanisms without direct observations of the full three-dimensional wind field and density structure of the MABL, which is currently not available over the Southern Ocean. This study therefore documents only the effects that SST fronts have on the surface wind stress field.

3. Data description

The wind stress and SST data analyzed here span the 2-yr period from 1 August 1999 to 31 July 2001, which corresponds to the first two complete years of the QuikSCAT scatterometer mission. For this analysis, we consider the Southern Ocean region between the latitudes 30° and 60°S. The wind stress and SST data are described in detail in this section.

The SeaWinds scatterometer onboard the QuikSCAT satellite infers surface wind stress magnitude and direction from measurements of microwave radar backscatter received from a given location on the sea surface at multiple antenna look angles (Freilich et al. 1994). Scatterometer wind stress retrievals are calibrated to the neutral-stability wind at a height of 10 m above the sea surface. The vector wind stress $\boldsymbol{\tau}$ is obtained from the 10-m neutral-stability wind $\mathbf{v}_{10}^N$ by $\boldsymbol{\tau} = \rho C_d^N \mathbf{v}_{10}^N |\mathbf{v}_{10}^N|$, where ρ is the air density and C_d^N is the neutral-stability drag coefficient (e.g., Large and Pond 1981). The QuikSCAT measurements have a 25-km resolution over a single 1600-km swath centered on the satellite ground track.

In this analysis, the QuikSCAT wind stress measurements have been smoothed and interpolated onto a 1° longitude by 1° latitude spatial grid at 7-day intervals using a locally weighted regression (loess) smoother (Schlax et al. 2001) with filter cutoff wavelengths of 2° latitude by 4° longitude and a filter cutoff period of 15 days. This filtering is similar to 1.2° latitude by 2.4° longitude by 9-day block averages. Except in raining conditions, the atmosphere is nearly transparent at microwave frequencies. The persistent cloud cover over the Southern Ocean therefore does not degrade the accuracy of the scatterometer estimates of surface wind stress in nonprecipitating conditions.

The accuracy of the QuikSCAT scatterometer measurements of 10-m winds has been extensively investigated by M. Freilich (2002, personal communication). Briefly, the QuikSCAT measurement accuracy is best characterized in terms of random component errors of the 10-m neutral-stability vector wind retrievals (Freilich and Dunbar 1999). The measurement errors have been found to be about 1.3 m s^{-1} for each orthogonal component with no significant dependence on wind speed. The wind speed accuracy is thus about 1.8 m s^{-1} over the full range of wind speeds, and the directional uncertainty decreases rapidly with increasing wind speed. Additionally, there is no evidence of systematic SST-dependent measurement errors in the QuikSCAT data.

Radar backscatter from sea ice results in large apparent wind speed, which causes spurious values of the derivative wind stress fields near the Antarctic ice edge. Wind stress and SST poleward of the northernmost extent of the sea ice over the 2-yr period were therefore eliminated from the analysis presented here. The sea ice edge information was provided by M. Freilich based on brightness temperature measurements by the Special Sensor Microwave Imager (SSM/I) flown onboard the Defense Meteorological Satellite Program satellites. The ice-contaminated region excluded from the 2-yr analysis period is shown in gray in Fig. 1.

The analysis of ocean–atmosphere coupling in the eastern tropical Pacific by Chelton et al. (2001) and others utilized the TRMM TMI for all-weather measurements of SST. Because of the low inclination of the TRMM satellite orbit, the TMI measures SST only in the latitude range between 38°S and 38°N. Most of the Southern Ocean region of interest in this study lies south of 38°S. Satellite microwave measurements of SST will soon become available at these higher latitudes from an Advanced Microwave Scanning Radiometer (AMSR) on the Earth Observing System (EOS) satellite *Aqua* launched in April 2002 and a second AMSR on the *Advanced Earth Observing Satellite-II* (*ADEOS-II*) launched in December 2002. Since microwave measurements of SST are not yet available for the Southern Ocean, the present study uses SST fields produced by NOAA based on the optimum interpolation technique described by Reynolds and Smith (1994).

The so-called Reynolds weekly average SST analyses blend all available in situ moored buoy and ship observations of SST with satellite infrared SST observations from the Advanced Very High Resolution Radiometer (AVHRR) on the NOAA series of polar-orbiting satellites. The SST analyses first apply the blending technique described by Reynolds (1988) and Reynolds and Marsico (1993) using input fields of in situ and AVHRR SST data. The blending effectively uses satellite SST data to define the SST gradient field in regions with sparse in situ data. The final SST fields are then obtained by adjusting the gradient fields to the in situ SST observations to remove large-scale biases in the satellite data. This blending technique results in a deg-

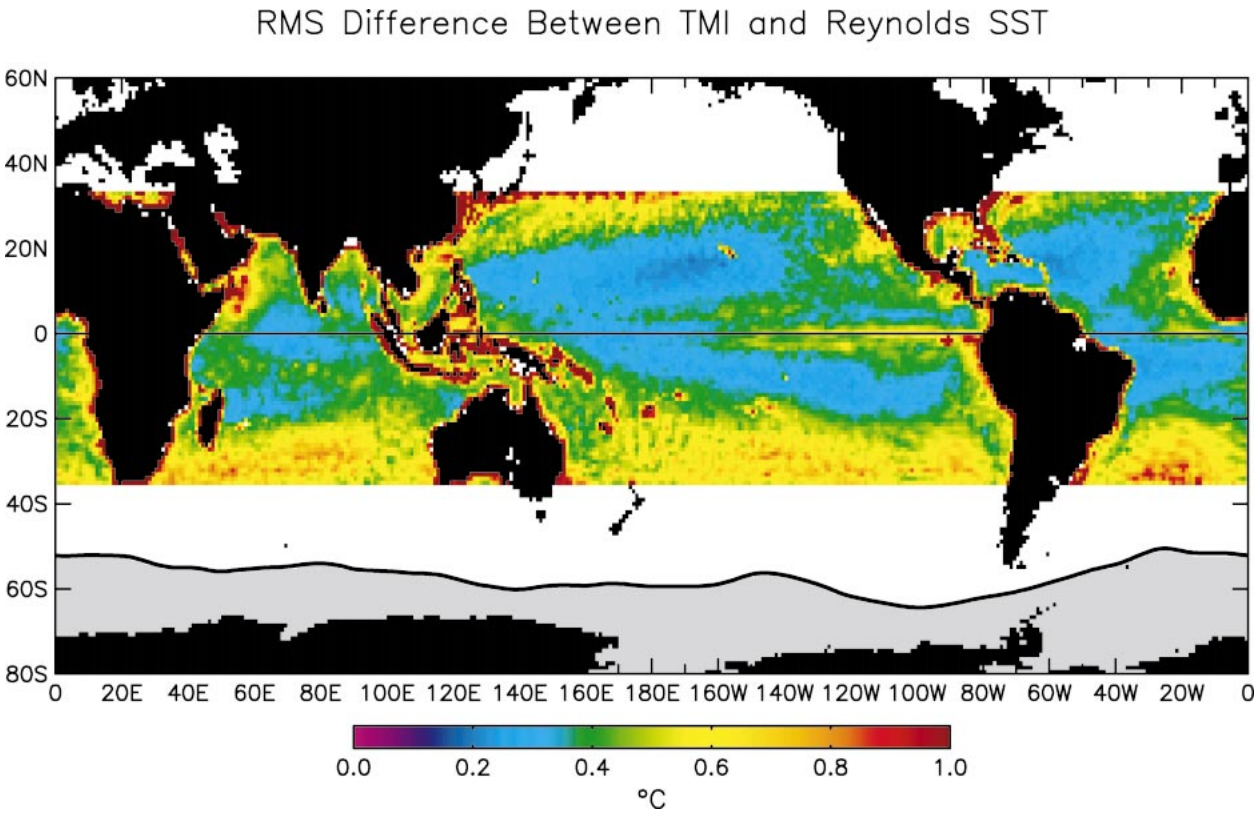

FIG. 1. A global map of the root-mean-square (rms) difference between the weekly averaged TMI SST and the weekly averaged Reynolds SST analyses. Also shown is the northernmost extent of the Antarctic sea ice over the analysis region for the period 1 Aug 1999–31 Jul 2001. The area masked from the analysis in shaded in gray.

radation of the spatial resolution to roughly 6° latitude by 6° longitude (Reynolds and Smith 1994).

In order to improve the resolution of the SST analyses, Reynolds and Smith (1994) used optimum interpolation (OI) to attempt to preserve the resolution capabilities of the satellite infrared SST. The OI technique described by Reynolds and Smith (1994) first uses the coarse-resolution SST fields derived from the blending to provide a large-scale correction to the satellite SST retrievals. The SST estimates are obtained from the OI analysis of in situ and corrected satellite SST data on a 1° latitude by 1° longitude spatial grid. Optimum interpolation apparently allows improved spatial resolution of SST over the blended fields while retaining the benefit of bias reduction in the satellite measurements provided by the blending technique.

Two main problems affect the quality of the Reynolds SST analyses in the Southern Ocean. The first is sparse AVHRR sampling owing to persistent cloud coverage over the Southern Ocean region of interest in this study where the annual mean cloud amount exceeds 75% (Rossow and Schiffer 1991; Hahn et al. 1995). The second is sparse in situ sampling because of the small number of standard shipping routes poleward of 30°S. The sparse sampling of both datasets raises serious concerns about the quality of the Reynolds SST analyses in the Southern Ocean region. In situ sampling is especially poor at the highest southern latitudes, where Antarctic resupply ships crossing the Antarctic Circumpolar Current during the austral summer provide nearly all of the yearly in situ SST measurements poleward of 50°S.

Reynolds and Marsico (1993) noted another problem affecting the blending technique in vast areas of the Southern Ocean. Differences between the AVHRR day and night cloud detection algorithms cause a warm bias in the averages of the satellite SST retrievals. Greater confidence is instilled in the daytime cloud screen, which uses both visible and infrared satellite observations to identify clouds; the daytime cloud screen accepts 3 times more observations than the nighttime cloud screen, which is based only on infrared observations. Reynolds and Marsico (1993) suggest that the resulting SST estimates are not representative of the average daily SST, but are biased toward the more numerous and warmer daytime temperatures, thus resulting in SST estimates that were too warm over much of the Southern Ocean.

In an attempt to reduce the bias in the satellite SSTs, Reynolds and Marsico (1993) include the assimilation of sea ice data from the National Meteorological Center to estimate the physical location of the sea ice boundary. At the ice edge, they impose an external boundary con-

dition in the blending algorithm that sets the SST to −1.8°C, which is the freezing temperature of seawater at a salinity of 32.86 psu. The inclusion of this ice edge temperature as a boundary condition in the blended analyses reduces the warm bias over large portions of the Southern Ocean. The assumption of an SST value of −1.8°C at the ice edge is likely to be adequate during freezing conditions. However, during the melt season and in regions of low ice concentrations, this assumption may lead to an underestimation of the SST by several tenths of a degree Celsius, since freshwater stratifies the surface seawater, leading to a heating of only a very thin layer at the surface. Uncertainty in the precise location of the ice edge will also cause uncertainty in the SST.

Despite the limitations summarized above, the Reynolds SST analyses provide the best SST estimates presently available poleward of 38°S. In an attempt to assess the quality of these SST fields, the root-mean-square (rms) differences between weekly averaged TMI SST and the Reynolds weekly average SST analyses are shown in Fig. 1. The largest differences occur near the highest latitudes sampled by the TMI. Some of these differences may be attributable to errors in the TMI SST (Stammer et al. 2003); however, most are likely due to errors in the Reynolds SST analyses and from the spatial smoothing inherent in the Reynolds blending algorithm as summarized earlier. This is especially a concern in the Southern Ocean region of interest here, since the rms difference exceeds 0.7°C poleward of 30°S where in situ SST data are sparse and the nearly ubiquitous cloud cover masks the infrared satellite SST retrievals. As discussed by Emery et al. (2001), there is a legitimate and pressing need for a comprehensive SST validation program, particularly in the region poleward of 30°S.

To mitigate the random errors that surely exist in the Reynolds SST analyses, the weekly analyses were averaged here in overlapping 3-month blocks at monthly intervals from 1 August 1999 to 31 July 2001 for the latitude band 30°–60°S. The overall average over this 2-yr period is contoured in Fig. 2a. Contours of the climatological average dynamic height relative to 1000-m depth from Levitus and Boyer (1994) are overlaid on the 2-yr average SST in Fig. 2b. Over the geographical region shown in this figure, the correlation between the 2-yr average SST and climatological average dynamic height is 0.91. The close agreement between these two fields implies that isotherms in the Reynolds SST analyses closely correspond to streamlines of the large-scale mean surface flow of the Antarctic Circumpolar Current (ACC) as represented by the climatological average dynamic height. The average Reynolds SST analyses evidently resolve most of the features of the mean surface circulation. The large, steady meanders in the flow result from the interactions between the mean current and bathymetry and are relatively stationary (Chelton et al. 1990). Moreover, the 2-yr averaging period considered here is evidently representative of long-term climatological average conditions in the Southern Ocean.

To be consistent with the smoothed Reynolds SST fields analyzed here, the QuikSCAT wind stress fields were also averaged in overlapping 3-month blocks at monthly intervals over the same 2-yr period from 1 August 1999 to 31 July 2001. The vector average wind stress field measured from QuikSCAT over the 2-yr period is overlaid on the 2-yr average Reynolds SST in Fig. 2c. The wind stress vectors are predominately westerly as expected within this latitude band in proximity to the Southern Hemisphere midlatitude surface westerly wind maximum. It is significant to note that the winds blow obliquely across the meandering isotherms in many places throughout the Southern Ocean. This provides ample opportunity to investigate whether wind stress curl and divergence perturbations occur in association with the underlying SST gradient field as observed by Chelton et al. (2001) in the eastern tropical Pacific.

4. Methods

a. Geometric relation between the wind stress and the SST gradient

The total SST gradient vector can be decomposed into local crosswind and downwind components. In vector notation, the cross product $(\nabla T \times \hat{\boldsymbol{\tau}}) \cdot \mathbf{k} = |\nabla T| \sin\theta$ represents the crosswind component, where T is the SST, $\hat{\boldsymbol{\tau}}$ is a unit vector in the direction of the wind stress, $\mathbf{k}$ is a unit vector in the vertical direction, and θ is the counterclockwise angle between the vectors ∇T and $\hat{\boldsymbol{\tau}}$. The vector dot product $\nabla T \cdot \hat{\boldsymbol{\tau}} = |\nabla T| \cos\theta$ is the projection of ∇T onto $\hat{\boldsymbol{\tau}}$ and represents the downwind component of the SST gradient.

As summarized in section 2, previous observations have found that the wind stress magnitude changes across SST fronts in response to changes in surface forcing caused by spatial gradients in SST. A schematic of winds blowing obliquely across a hypothetical meandering SST front is shown in Fig. 3. When the crosswind SST gradient is nonzero, the lateral (crosswind) gradient of wind stress that develops as the winds increase over the warmer water results in a curl of the wind stress. Likewise, when the downwind SST gradient is nonzero, the longitudinal (downwind) deceleration or acceleration across the front results in a convergence or divergence of the wind stress. The wind stress curl and divergence should therefore depend, respectively, on the magnitudes of the crosswind and downwind SST gradients.

At $\theta = 0°$, the wind blows across isotherms (parallel to the SST gradient) toward warmer water. The increased wind stress over the warmer water should result in a maximum in the divergence, while the curl should vanish. At $\theta = 180°$, there should be a maximum convergence and zero wind stress curl. Conversely, at $\theta =$

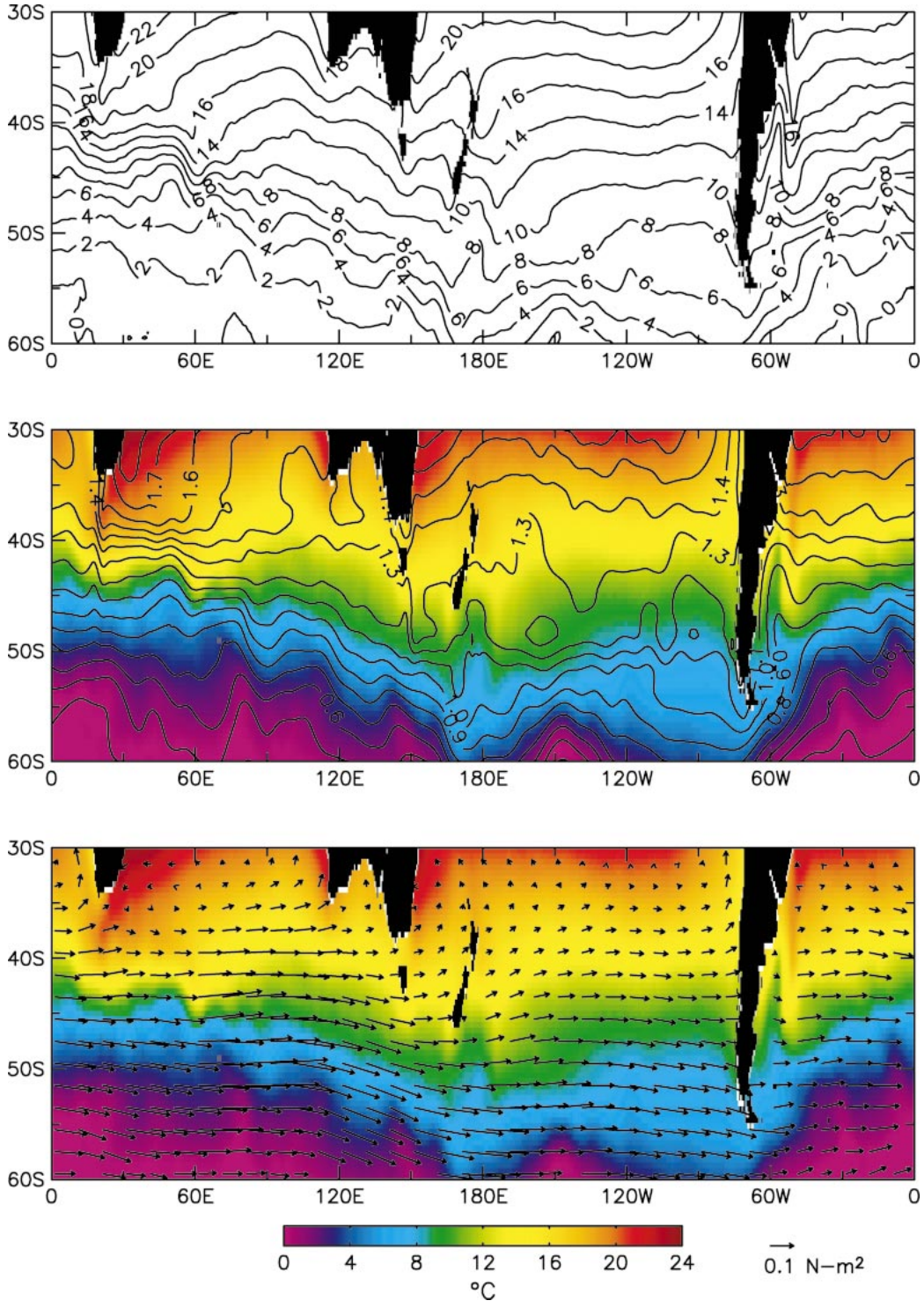

FIG. 2. Averages over the 2-yr period 1 Aug 1999–31 Jul 2001: (top) Reynolds SST analyses; (middle) contours of the climatological average dynamic height relative to 1000-m depth from Levitus and Boyer (1994) with the 2-yr average SST shown in color according to the scale at the bottom; (bottom) vector average wind stress from QuikSCAT overlaid on the 2-yr average SST.

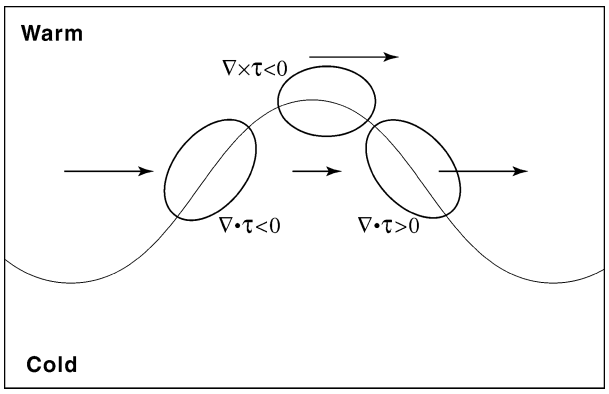

FIG. 3. Schematic of the hypothesized interaction between wind stress and SST for wind blowing obliquely across a meandering SST front. The SST front is delineated as the black sinusoidal curve, separating warm and cold water. The lengths of the arrows schematically represent the hypothesized relative magnitudes of the surface wind stress. Regions of nonzero wind stress curl and divergence are indicated.

90°, the wind blows along isotherms (perpendicular to the SST gradient) with warmer water to the right of the wind and colder water to the left. In response, a maximum positive wind stress curl should develop, while the divergence should vanish. At $\theta = 270°$, there should be a maximum negative wind stress curl and zero divergence. These anticipated relations between the derivative wind stress fields and the SST gradient field are investigated quantitatively in section 5.

b. Spatial filtering of the wind stress fields

Confirmation of the hypothesized relations between the derivative wind stress fields and the angle between the wind stress and the SST gradient requires the removal of other signals in the wind field that are unrelated to the SST field. At the high southern latitudes of interest in this study, energetic synoptic-scale weather disturbances and the large-scale transverse gradient of the midlatitude mean westerly wind maximum dominate the wind stress curl field, masking perturbations that may exist in association with the SST gradients. The influence of transient synoptic-scale weather disturbances is mostly eliminated in the 3-month averages considered here. The influence of the large-scale background wind stress curl is evident in the 2-yr average wind stress curl field shown in Fig. 4 (top). The westerly wind varies meridionally and is maximum along the approximate axis of the ACC. The decrease of the westerly winds equatorward and poleward of this westerly wind maximum result in positive and negative wind stress curl on the north and south sides of the maximum, respectively. Removal of the strong curl associated with the mean westerly winds by spatial high-pass filtering is necessary to isolate the SST-induced perturbations of the wind stress curl field that are of interest here.

The large-scale wind stress curl field obtained by applying a spatial low-pass filter to isolate variability with wavelengths longer than 10° latitude by 30° longitude is shown in Fig. 4 (middle). Although these filter cutoff wavelengths are roughly equivalent to those of simple 6° latitude by 18° longitude block averages, the two-dimensional loess smoother used here has a more desirable filter transfer function (see Fig. 1 of Chelton and Schlax 2003). The precise choice of the filter cutoff wavelengths does not greatly influence the results of the analysis presented here.

Figure 4 (bottom) shows the 2-yr average spatially high-pass-filtered curl fields obtained by subtracting the $10° \times 30°$ spatially smoothed curl field from the unfiltered curl field, thus retaining spatial variability with wavelengths shorter than 10° latitude by 30° longitude but longer than the $2° \times 4°$ wavelengths of the original smoothed wind stress fields. It is apparent that the high-pass-filtered curl field is most intense and spatially variable within a band centered along the axis of the ACC where SST gradients are strong [see the contours in Fig. 4 (bottom)]. Away from the ACC, the magnitudes of the short-scale curl perturbations are small. Visually, the magnitudes of the short-scale wind stress curl signals are as strong as the large-scale curl shown in Fig. 4 (middle). The implications this has on the local ocean circulation are discussed in section 6.

The 2-yr average wind stress divergence and SST fields for the Southern Ocean are shown in Fig. 5 (top). Like the curl, the divergence exhibits patchy spatial variability within the band of strong SST gradients centered on the axis of the ACC. Figure 5 (middle) shows the spatially low-pass-filtered divergence field, which was obtained in the same way as the large-scale curl field in Fig. 4 (middle). In contrast with the curl field, the magnitude of the spatially low-pass-filtered divergence is small everywhere, reflecting the inherent tendency for the wind stress field to be nearly nondivergent. Consequently, the spatially high-pass-filtered wind stress divergence in Fig. 5 (bottom) differs little from the unfiltered wind stress divergence at the top of the figure.

The spatial high-pass filtering shown in the bottom panels of Figs. 4 and 5 for the 2-yr average from August 1999 to July 2001 was applied to each of the overlapping 3-month average curl and divergence fields for the analyses in section 5. These spatially high-pass-filtered curl and divergence fields are referred to hereafter as the perturbation wind stress curl and divergence.

The crosswind and downwind SST gradient fields were spatially high-pass-filtered in the same manner as the wind stress curl and divergence fields. In vector notation, $(\boldsymbol{\nabla} T \times \hat{\boldsymbol{\tau}})' \cdot \mathbf{k}$ and $(\boldsymbol{\nabla} T \cdot \hat{\boldsymbol{\tau}})'$ denote the spatially high-pass-filtered crosswind and downwind SST gradients, respectively. These represent the contributions of the SST gradient field hypothesized to induce the perturbations in the wind stress curl and divergence fields under investigation in this study. Since the perturbation wind stress curl and divergence are expected to depend on the perturbation crosswind and downwind

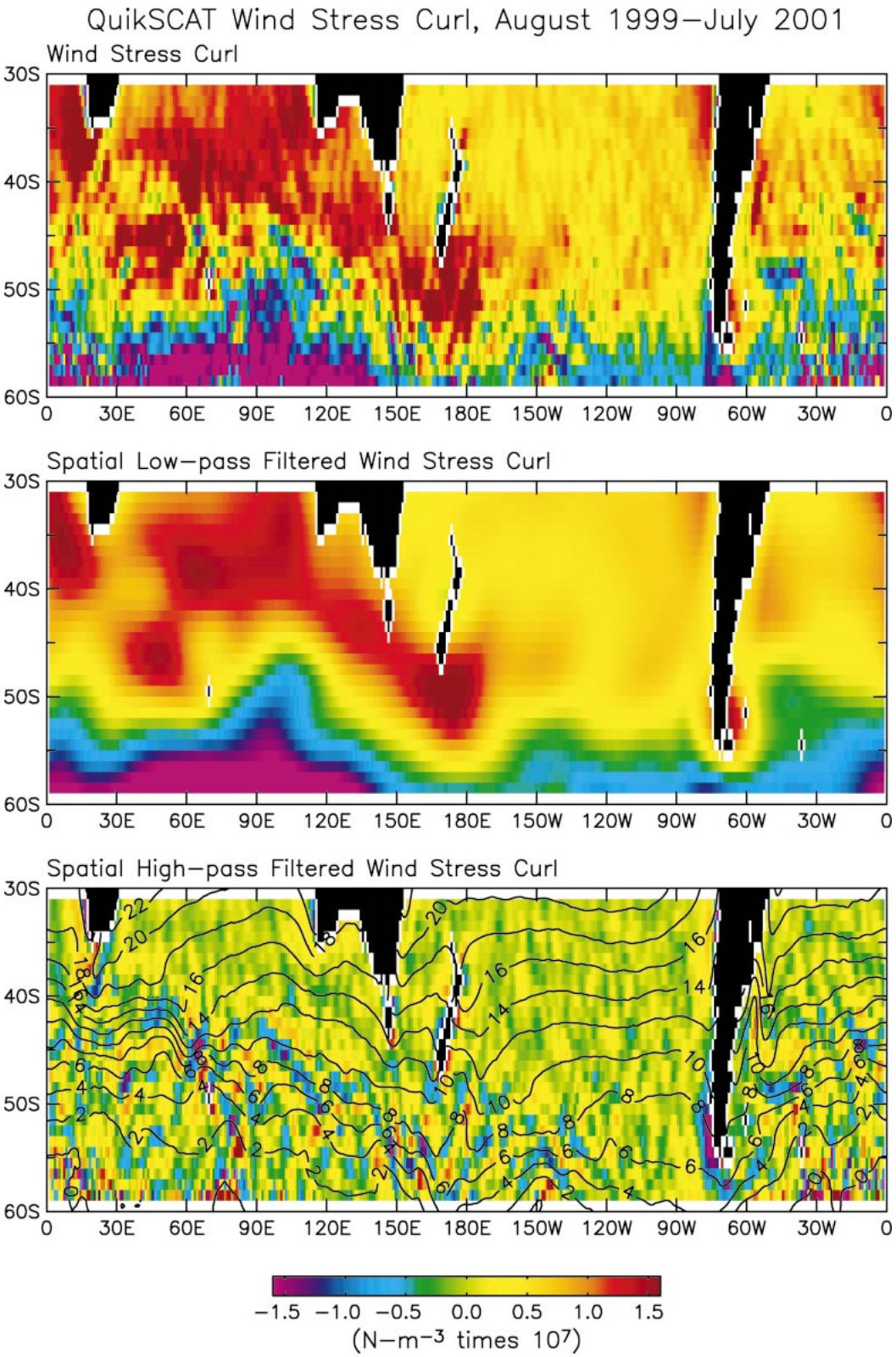

FIG. 4. Average maps over the 2-yr period 1 Aug 1999–31 Jul 2001: (top) wind stress curl; (middle) spatially smoothed wind stress curl with wavelengths longer than 10° latitude by 30° longitude; (bottom) spatially high-pass-filtered wind stress curl with wavelengths shorter than 10° latitude by 30° longitude; the contours overlaid are the 2-yr average SST from Fig. 2a with a contour interval of 1°C.

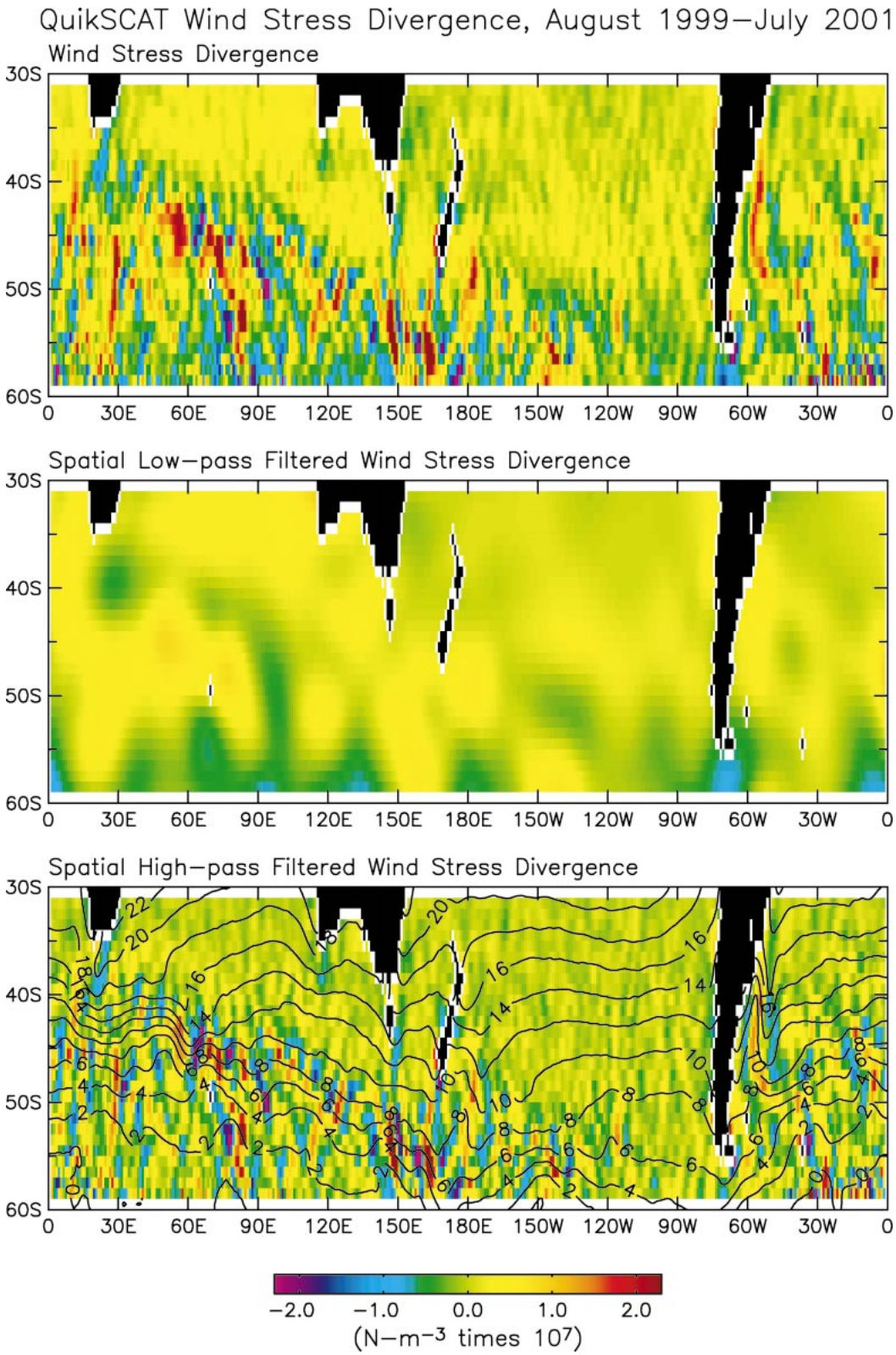

FIG. 5. Same as in Fig. 4 except for the wind stress divergence.

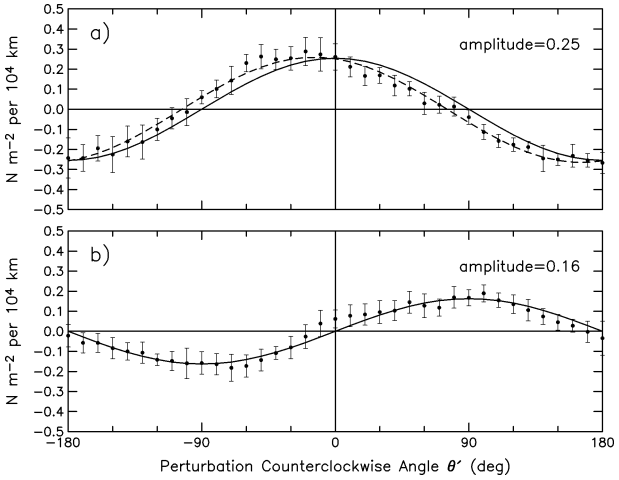

FIG. 6. Binned scatterplots of the angular dependencies of (a) perturbation wind stress divergence, $\nabla \cdot \hat{\boldsymbol{\tau}}'$, and (b) perturbation wind stress curl, $\nabla \times \hat{\boldsymbol{\tau}}' \cdot \mathbf{k}$ on the perturbation angle θ' defined by Eq. (1). The points in (a) and (b) are the means within each bin computed from 11 overlapping 3-month averages over the 2-yr analysis period, and the error bars represent ± 1 std dev of the means within each bin. The solid lines in (a) and (b) represent least squares fits to a sine and a cosine, respectively. The dashed curve in (a) is the least squares fit to a sinusoid, which is shifted 23° clockwise relative to a cosine of zero phase.

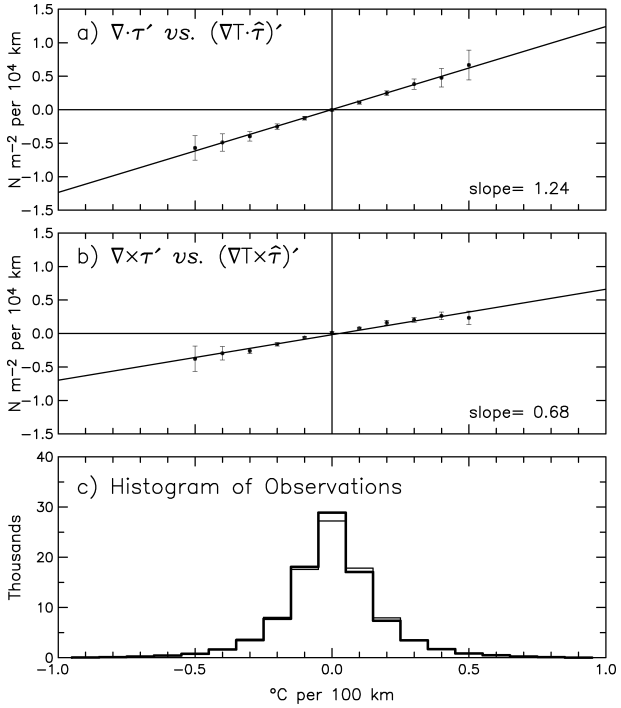

FIG. 7. Binned scatterplots of the relationships between the spatially high-pass-filtered SST and wind stress fields: (a) the perturbation wind stress divergence, $\nabla \cdot \hat{\boldsymbol{\tau}}'$, plotted as a function of the perturbation downwind SST gradient, $(\nabla T \cdot \hat{\boldsymbol{\tau}})'$; (b) the perturbation wind stress curl, $\nabla \times \hat{\boldsymbol{\tau}}' \cdot \mathbf{k}$, plotted as a function of the perturbation crosswind SST gradient, $(\nabla T \times \hat{\boldsymbol{\tau}})' \cdot \mathbf{k}$; and (c) histograms of the number of observations within each bin for (a) (thick line) and (b) (thin line). The points in (a) and (b) are the means within each bin computed from the 11 individual 3-month averages, and the error bars are ± 1 std dev of the means within each bin. The lines through the points represent least squares fits of the binned overall means to straight lines.

SST gradients, they should depend, respectively, on the sine and cosine of the perturbation angle defined by

$$\theta' = \tan^{-1}\left[\frac{(\nabla T \times \hat{\boldsymbol{\tau}})' \cdot \mathbf{k}}{(\nabla T \cdot \hat{\boldsymbol{\tau}})'}\right]. \qquad (1)$$

5. Results

The perturbation curl and divergence fields for the Southern Ocean were binned as functions of the perturbation angle θ' defined by (1) for each of the 11 overlapping 3-month average fields over the 2-yr period 1 August 1999–31 July 2001. The overall averages within each bin are shown as the points in Fig. 6. The error bars represent ± 1 standard deviation of the means within each bin computed from the 11 individual 3-month averages. As in the tropical study by Chelton et al. (2001), the Southern Ocean QuikSCAT perturbation curl and divergence fields agree remarkably well with the expected sine and cosine dependencies on θ'. The solid curves represent least squares fits of a sine and cosine to the overall binned averages. The perturbation curl is maximum when the wind vector is perpendicular to the SST gradient (parallel to isotherms) and zero when the wind vector is parallel to the SST gradient (perpendicular to isotherms). Likewise, the perturbation divergence or convergence is approximately largest when the wind vector is oriented parallel to the SST gradient (perpendicular to isotherms) and approximately zero when the wind vector is oriented perpendicular to the SST gradient (parallel to isotherms).

An interesting feature of the perturbation divergence dependence on θ' is that the sinusoidal variation of the divergence is shifted slightly relative to a pure cosine. The wind stress divergence is maximum when the wind direction is 23° clockwise relative to the SST gradient. This is discussed further in section 6.

While the relationships shown in Fig. 6 clarify the dependencies of the perturbation curl and divergence fields on the perturbation angle θ', the magnitude of the curl and divergence responses to a given SST gradient cannot be inferred from these binned averages as a function of θ'. The perturbation curl and divergence binned as functions of the perturbation crosswind and downwind components of the SST gradient, respectively, are shown in Fig. 7. The perturbation curl and divergence exhibit linear, positive trends with the perturbation crosswind and downwind SST gradient, respectively, consistent with the hypothesis discussed in section 4 and with the results found in the eastern tropical Pacific by Chelton et al. (2001). The solid line represents a linear least squares fit to the binned averages. Probably coincidentally, the slopes of the lines in Fig. 7, denoted

TABLE 1. The coupling coefficients computed in this analysis over the Antarctic Circumpolar Current (ACC) and the values computed by Chelton et al. (2001) over the eastern tropical Pacific (ETP) during the period 21 Jul to 20 Oct 1999. The coupling coefficient α_D represents the linear relation between the wind stress divergence and the downwind component of the SST gradient (Fig. 7a). The coupling coefficient α_C represents the linear relation between the wind stress curl and the crosswind component of the SST gradient (Fig. 7b). The units are N m^{-2} °C^{-1} × 100.

Location	α_D	α_C
ACC	1.24	0.68
ETP (1°–5°S)	2.47	1.12
ETP (3°N–1°S)	1.35	0.75

here as the coupling coefficient α_C for the curl and α_D for the divergence, are quite close to those obtained between 3°N and 1°S in the eastern tropical Pacific by Chelton et al. (2001; see Table 1). Notably, α_D is about double the value of α_C in both regions.

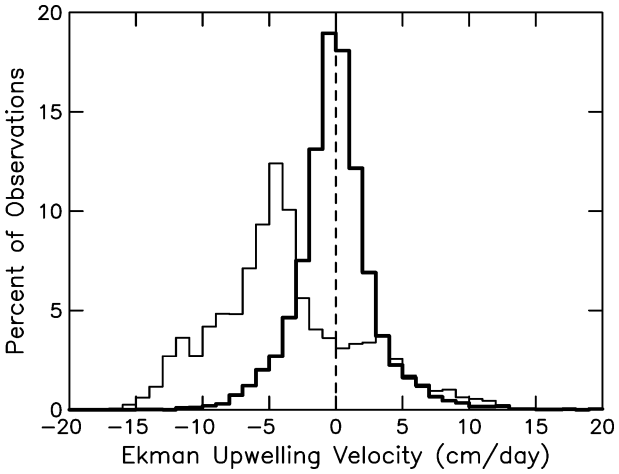

FIG. 8. Histograms of the Ekman pumping calculated from the spatially low-pass-filtered wind stress curl field (thin line), and from the spatially high-pass-filtered wind stress curl field (heavy line). Units are cm day^{-1}.

6. Discussion and conclusions

The coupling between SST and the lower atmosphere has been studied extensively in the eastern tropical Pacific (e.g., Wallace et al. 1989; Hayes et al. 1989; Xie et al. 1998; Chelton et al. 2001; Liu et al. 2000; Hashizume et al. 2001; Polito et al. 2001). Several case studies based on in situ observations (Sweet et al. 1981; Jury and Walker 1988; Jury 1994; Rouault and Lutjeharms 2000) and on satellite scatterometer data (Rouault and Lutjeharms 2000; Nonaka and Xie 2003) have documented similar coupling in midlatitudes. The present study is the first to quantify this coupling statistically over the entire Southern Ocean, which encompasses nearly 25% of the World Ocean. The emerging view that ocean–atmosphere coupling is a globally important phenomenon is only becoming fully appreciated with the availability of the multiyear data record of spatially and temporally dense observations of surface winds from the QuikSCAT scatterometer.

At the present time, the only SST fields available for investigation of SST perturbations of surface winds at latitudes higher than 38°S are the Reynolds SST analyses produced by NOAA (Reynolds and Smith 1994). As summarized in section 3, these SST fields are unquestionably the weakest part of the present analysis, although temporally averaging the Reynolds SST analyses over 3-month periods for the analysis presented here addresses some of the concerns about their accuracies over the Southern Ocean. The high correlation between the 2-yr average SST field and the long-term average dynamic height field instills some confidence that the Reynolds SST analyses are adequate in sufficiently long-term temporal averages. The existence of persistent meanders in the flow of the ACC and in the associated SST field thus allow an investigation of the effects of SST on the 2-yr mean wind stress fields observed by QuikSCAT.

The spatially high-pass-filtered wind stress and SST fields used in this study isolate the short-scale perturbations of interest here with zonal and meridional wavelengths shorter than 10° latitude by 30° longitude and longer than 2° latitude by 4° longitude. The spatial variability in the spatially high-pass-filtered derivative wind stress fields considered here is largest within a broad band centered along the axis of the ACC between 40° and 50°S. The spatial structures of these perturbation derivative wind stress fields were shown to be remarkably closely related to the perturbations of the SST field throughout the Southern Ocean.

The surface observations analyzed here cannot elucidate the details of the boundary layer dynamics and thermodynamics of SST modification of low-level winds. However, the observed coupling is consistent with the hypothesis of Sweet et al. (1981) and Wallace et al. (1989) that SST modification of the MABL produces changes in stability that cause variations in the surface winds through vertical turbulent transfer of momentum to the surface.

The magnitudes of short-scale variability in the wind stress curl field are qualitatively seen from the bottom and middle panels of Fig. 4 to be comparable to the magnitudes of the background large-scale curl field itself. To quantify the effects that this has on the upper ocean, histograms of the wind stress curl-induced Ekman pumping velocity were calculated separately from the spatially high-pass-filtered and spatially low-pass-filtered 2-yr average curl fields (Fig. 8). Though shifted to have zero mean value, the dynamic range of values of the Ekman pumping velocity calculated from the perturbation curl field is nearly as broad as that of the background large-scale curl field. The perturbation curl field associated with the persistent perturbation crosswind temperature gradients therefore produces a local ocean response comparable to that associated with the

large-scale wind forcing. This suggests a coupling whereby SST gradients drive an atmospheric response that feeds back on the SST through Ekman pumping. Modeling studies are needed to determine whether this feedback tends to reinforce or reduce the SST gradient that is responsible for the perturbations of the wind stress curl field. The steady short-scale variability of the Ekman pumping field may also have locally significant biological consequences that merit detailed investigation.

It was noted in section 5 that the magnitude of the coupling between the perturbation wind stress curl field and the underlying SST field is somewhat weaker than that of the perturbation wind stress divergence (see Table 1). This was also found to be the case in the eastern tropical Pacific (Chelton et al. 2001). The difference between the magnitudes of the coupling coefficients α_C and α_D suggests that a different combination of mechanisms could be responsible for the perturbation divergence response to downwind SST gradients than for the perturbation curl response to crosswind SST gradients. Without knowledge of the full three-dimensional wind and density fields in the MABL, we can only speculate about the mechanisms responsible for the different coupling coefficients.

One possible explanation for the stronger response of the wind stress divergence to the downwind SST gradient compared with the wind stress curl response to the crosswind SST gradient is the finite timescale of boundary layer adjustment to the surface SST boundary condition. For flow across an SST front, a parcel of air experiences a continually changing SST boundary condition. Convective and turbulent fluxes are therefore not able to reach their equilibrium values. As suggested by Chelton et al. (2001), this would result in divergence or convergence that is stronger than would be the case for an equilibrated boundary layer structure. In the case of flow along an SST front, the weak downwind SST gradient may allow sufficient time for equilibration adjustment of the boundary layer, thus resulting in a wind stress curl that is weaker than would be the case for a nonequilibrated boundary layer. Thum et al. (2002) found strong evidence that a disequilibrium boundary layer is responsible for a spatial shift between the surface heat fluxes and perturbation SSTs associated with TIWs in the eastern tropical Pacific.

Because scatterometers measure the wind stress relative to the moving sea surface (Cornillon and Park 2001; Kelly et al. 2001), ocean surface currents could also contribute to some of the apparent difference between the response of the perturbation wind stress divergence and curl fields to underlying perturbations in the SST field. Without coincident surface current observations, the effects that surface ocean currents have on the wind stress field cannot be directly quantified. Surface ocean currents in the Southern Ocean can easily be as strong as 0.5 m s^{-1}, which is a sizable fraction of the typical perturbation surface wind speed of 2–3 m s^{-1} in this region. The high correlation between the dynamic height and the SST fields implies that the surface ocean currents would most significantly affect the wind stress curl, which is strongest when the wind blows parallel to isotherms (i.e., parallel to the flow). Ocean currents would thus reduce the wind stress curl response to the crosswind SST gradients as observed from QuikSCAT, leading to smaller values of α_C compared with α_D.

The observational and modeling studies summarized in section 2 suggest a third possible mechanism for the difference between α_C and α_D. The increase of winds at the ocean surface is likely attributable to a mixture of the vertical turbulent transfer of momentum and the effects of secondary circulations across SST fronts. The turbulent transfer mechanism should produce equal responses of the curl and divergence fields to crosswind and downwind SST gradients. In contrast, secondary circulations would have little or no effect on the wind stress curl since the surface winds associated with the secondary circulations would be oriented in the cross-frontal direction. This efficaciously augments the effects of the SST gradient on the wind stress divergence relative to the wind stress curl. Surface air blowing obliquely across an SST front would accelerate more across the front than along it, leading to a larger wind stress divergence than wind stress curl for a given downwind SST gradient, thus explaining at least part of the larger values of α_D compared with α_C.

The existence of what we believe is a significant clockwise rotation of about 20° between the binned values of the perturbation divergence and the perturbation angle θ' in Fig. 6 (top) is further evidence that the observed air–sea interaction is more complex than just vertical turbulent mixing associated with SST modification of boundary layer stability. Chelton et al. (2001) found no evidence of such a rotation over the eastern equatorial Pacific. It is noteworthy that there is no evidence of a systematic phase shift between the binned values of the perturbation curl and the expected sine dependence on θ' [see Fig. 6 (bottom)]. The physical reason for the rotation in the divergence over the Southern Ocean is not yet clear. As shown in Fig. 9, it is linked to a negative, linear relation between the perturbation wind stress divergence and the perturbation crosswind SST gradient. It is conceivable that the crosswind SST gradient sets up a cross-frontal pressure gradient that causes a cross-frontal acceleration of the wind stress over the front. This contribution to the divergence could also arise from secondary circulations forcing an increase in cross-frontal winds as air flows along isotherms that perhaps influences the divergence more than the curl, thus resulting in the approximate 20° rotation in Fig. 6 (top). Further observational, analytical, and modeling studies are needed to fully understand this observation.

We close by reemphasizing our concern about the accuracies of the Reynolds SST fields. From a prelim-

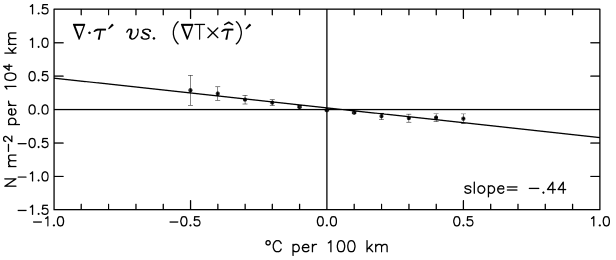

FIG. 9. Binned scatterplot of the relationship between the perturbation wind stress divergence and the perturbation crosswind SST gradient. The points are the means within each bin computed from the 11 individual 3-month averages, and the error bars are ±1 std dev within each bin. The sloped line represents a least squares fit of the binned overall means to a straight line.

inary analysis of SST data from the AMSR on the EOS satellite *Aqua*, the spatial scales of the SST variability are overly smooth and the magnitude of SST gradients within a broad band centered on the ACC are significantly underestimated in the Reynolds SST fields. The actual coupling between SST and the overlying wind stress field is therefore stronger than has been deduced here from the QuikSCAT winds and the Reynolds SST analyses. The coupling coefficients presented in Fig. 7 of section 5 are therefore likely to need refinement as the AMSR observations accumulate to a sufficiently long data record to allow a quantitative analysis of air–sea coupling over the Southern Ocean.

Acknowledgments. We thank Michael Freilich for the QuikSCAT data and the ice field information and Michael Schlax for producing the smoothed QuikSCAT and Reynolds SST fields used in this study and for many helpful discussions throughout the course of this study. We also thank Michael Freilich for providing detailed helpful comments on this manuscript. The research presented in this paper was supported by NASA Grant NAS5-32965 for funding of Ocean Vector Winds Science Team activities and Grant NA96GP0368 from the NOAA Office of Global Programs.

REFERENCES

Chelton, D. B., M. G. Schlax, D. L. Witter, and J. G. Richman, 1990: Geosat altimeter observations of the surface circulation of the Southern Ocean. *J. Geophys. Res.,* **95,** 17 877–17 904.

——, and Coauthors, 2001: Observation of coupling between surface wind stress and sea surface temperature in the eastern tropical Pacific. *J. Climate,* **14,** 1479–1498.

——, and M. G. Schlax, 2003: The accuracies of smoothed sea surface height fields constructed from tandem altimeter datasets. *J. Atmos. Ocean Technol.,* in press.

Cornillon, P., and K.-A. Park, 2001: Warm core ring velocities inferred from NSCAT. *Geophys. Res. Lett.,* **28,** 575–578.

Deser, C., J. J. Bates, and S. Wahl, 1993: The influence of sea surface temperature on stratiform cloudiness along the equatorial front in the Pacific Ocean. *J. Climate,* **6,** 1172–1180.

Emery, W. J., S. Castro, G. A. Wick, P. Schluessel, and C. J. Donlon, 2001: Estimating sea surface temperature from infrared satellite and in situ temperature data. *Bull. Amer. Meteor. Soc.,* **82,** 2773–2784.

Freilich, M. H., and R. S. Dunbar, 1999: The accuracy of the NSCAT-1 vector winds: Comparisons with National Data Buoy Center buoys. *J. Geophys. Res.,* **104,** 11 231–11 246.

——, D. G. Long, and M. W. Spencer, 1994: SeaWinds: A scanning scatterometer for ADEOS II—Science overview. *Proc. Int. Geoscience and Remote Sensing Symp.,* Pasadena, CA, IEEE, 960–963.

Hahn, C. J., S. G. Warren, and J. London, 1995: The effect of moonlight on observation of cloud cover at night, and application to cloud climatology. *J. Climate,* **8,** 1429–1446.

Hashizume, H., S.-P. Xie, W. T. Liu, and K. Takeuchi, 2001: Local and remote atmospheric response to tropical instability waves: A global view from space. *J. Geophys. Res.,* **106,** 10 173–10 185.

——, ——, M. Fujiwara, M. Shiotani, T. Watanabe, Y. Tanimoto, W. T. Liu, and K. Takeuchi, 2002: Direct observations of atmospheric boundary layer response to slow SST variations over the eastern equatorial Pacific. *J. Climate,* **15,** 3379–3393.

Hayes, S. P., M. J. McPhaden, and J. M. Wallace, 1989: The influence of sea surface temperature on surface wind in the eastern equatorial Pacific: Weekly to monthly variability. *J. Climate,* **2,** 1500–1506.

Hsu, S. A., 1984: Sea-breeze-like winds across the north wall of the Gulf Stream: An analytical model. *J. Geophys. Res.,* **89,** 2025–2028.

Jury, M. R., 1994: A thermal front within the marine atmospheric boundary layer over the Agulhas Current south of Africa: Composite aircraft observations. *J. Geophys. Res.,* **99,** 3297–3304.

——, and N. Walker, 1988: Marine boundary layer modification across the edge of the Agulhas Current. *J. Geophys. Res.,* **93,** 647–654.

Kelly, K. A., S. Dickinson, M. J. McPhaden, and G. C. Johnson, 2001: Ocean currents evident in satellite wind data. *Geophys. Res. Lett.,* **28,** 2469–2472.

Large, W. G., and S. Pond, 1981: Open ocean momentum flux measurements in moderate to strong winds. *J. Phys. Oceanogr.,* **11,** 324–336.

Levitus, S., and T. P. Boyer, 1994: *Temperature,* Vol. 4, *World Ocean Atlas 1994,* NOAA Atlas NESDIS 4, 117 pp.

Lindzen, R. S., and S. Nigam, 1987: On the role of sea surface temperature gradients in forcing low-level winds and convergence in the Tropics. *J. Atmos. Sci.,* **44,** 2418–2436.

Liu, W. T., X. Xie, P. S. Polito, S.-P. Xie, and H. Hashizume, 2000: Atmospheric manifestation of tropical instability waves observed by QuikSCAT and Tropical Rain Measuring Mission. *Geophys. Res. Lett.,* **27,** 2545–2548.

Nonaka, M., and S.-P. Xie, 2003: Covariations of sea surface temperature and wind over the Kuroshio and its extension: Evidence for ocean-to-atmosphere feedback. *J. Climate,* **16,** 1404–1413.

Polito, P. S., J. P. Ryan, T. W. Liu, and F. P. Chavez, 2001: Oceanic and atmospheric anomalies of tropical instability waves. *Geophys. Res. Lett.,* **28,** 2233–2237.

Reynolds, R. W., 1988: A real-time global sea surface temperature analysis. *J. Climate,* **1,** 75–86.

——, and D. C. Marsico, 1993: An improved real-time global sea surface temperature analysis. *J. Climate,* **6,** 114–119.

——, and T. M. Smith, 1994: Improved global sea surface temperature analyses using optimum interpolation. *J. Climate,* **7,** 929–948.

Rossow, W. B., and R. A. Schiffer, 1991: ISCCP cloud data products. *Bull. Amer. Meteor. Soc.,* **72,** 2–20.

Rouault, M., and J. R. E. Lutjeharms, 2000: Air–sea exchange over an Agulhas eddy at the subtropical convergence. *Global Atmos. Ocean Syst.,* **7,** 125–150.

Schlax, M. G., D. B. Chelton, and M. H. Freilich, 2001: Sampling errors in wind fields constructed from single and tandem scatterometer datasets. *J. Atmos. Oceanic Technol.,* **18,** 1014–1036.

Stammer, D., F. Wentz, and C. Gentemann, 2003: Validation of microwave sea surface temperature measurements for climate purposes. *J. Climate,* **16,** 73–87.

Sweet, W. R., R. Fett, J. Kerling, and P. LaViolette, 1981: Air–sea

interaction effects in the lower troposphere across the north wall of the Gulf Stream. *Mon. Wea. Rev.*, **109,** 1042–1052.

Thum, N., S. K. Esbensen, D. B. Chelton, and M. J. McPhaden, 2002: Air–sea heat exchange along the northern sea surface temperature front in the eastern tropical Pacific. *J. Climate,* **15,** 3361–3378.

Wai, W. M., and S. A. Stage, 1989: Dynamical analysis of marine atmospheric boundary layer structure near the Gulf Stream oceanic front. *Quart. J. Roy. Meteor. Soc.*, **115,** 29–44.

Wallace, J. M., T. P. Mitchell, and C. Deser, 1989: The influence of sea-surface temperature on surface wind in the eastern equatorial Pacific: Seasonal and interannual variability. *J. Climate,* **2,** 1492–1499.

Warner, T. T., M. N. Lakhtakia, J. D. Doyle, and R. A. Pearson, 1990: Marine atmospheric boundary layer circulations forced by Gulf Stream sea surface temperature gradients. *Mon. Wea. Rev.*, **118,** 309–323.

Xie, S.-P., M. Ishiwatari, H. Hashizume, and K. Takeuchi, 1998: Coupled ocean–atmosphere waves on the equatorial front. *Geophys. Res. Lett.*, **25,** 3863–3866.